Supporting Information

Defect-Engineered Cu_2O/Co_xO Heterostructures with Built-In Electric Fields for High-Current-Density Alkaline Water Splitting

Tingting Tang,[a] Zhendong Gao,[a] Kuoteng Sun,[c] Chenggong Niu,[a] Chenxi Shang,[a] Jingya Guo,[a] Jianniao Tian,*[a] Tayirjan Taylor Isimjan*[b] and Xiulin Yang*[a]

[a] *Guangxi Key Laboratory of Low Carbon Energy Materials, School of Chemistry and Pharmaceutical Sciences, Guangxi Normal University, Guilin 541004, China*

[b] *Saudi Arabia Basic Industries Corporation (SABIC) at King Abdullah University of Science and Technology (KAUST), Thuwal 23955-6900, Saudi Arabia*

[c] *Liuzhou Bureau of EHV Transmission Company of China Southern Power Grid Co. Ltd, Liuzhou 545006, China*

E-mail addresses: xlyang@gxnu.edu.cn (X. Yang), isimjant@sabic.com birdtjn@sina.com (J. Tian).

1. Experimental section

1.1 Materials characterizations

XRD measurements were performed using a Rigaku D/Max 2500 V/PC diffractometer with Cu Kα radiation (λ = 0.15406 nm) to determine the crystal structure of the catalysts. The morphological features and elemental information were obtained by field-emission scanning electron microscopy (FESEM, Quanta 200). Further structural details at the nanoscale were provided by transmission electron microscopy (TEM, Talos 200S). XPS analysis was performed on a Thermo Fisher Scientific Nexsa instrument (Mg Kα radiation) to probe the chemical states. Raman spectroscopy was conducted using a Renishaw in Via system equipped with a 785 nm laser. A Bruker E500 spectrometer was employed to record the electron paramagnetic resonance (EPR) spectra. The specific surface area and pore structure distribution were measured by a Quantachrome instrument (BET, BELSORP MaxII). Surface wettability, evaluated via water contact angle measurements, was determined using a DataPhysics OCA 15EC goniometer. Optical absorption properties were analyzed with a Shimadzu UV-3600i Plus UV-Vis spectrophotometer to derive the band gap. Additionally, the electronic valence band structure was probed by ultraviolet photoelectron spectroscopy (UPS) on a PHI5000 VersaProbe III spectrometer.

1.2 In situ spectroscopic characterizations

Electrochemical impedance spectroscopy (EIS) was conducted at constant applied potentials (0.95 - 1.45 V vs. RHE) with a 10-minute stabilization period at each potential. This approach enabled simultaneous monitoring of reaction dynamics and surface characteristics, with spectra recorded over a frequency range of 0.01 Hz to 300 kHz.

In situ Raman spectroscopy was carried out on a Renishaw InVia Qontor system to track the catalyst's evolution under applied potentials from 1.0 to 1.7 V (vs. RHE). The experiment utilized a Gaoss Union C031-1 electrochemical cell with a standard three-electrode setup (as-synthesized catalyst working electrode, carbon rod counter electrode, Ag/AgCl reference electrode) in 1.0 M KOH. All spectra were recorded with a 785 nm laser and a 10 s integration time.

The in-situ ATR-FTIR setup consisted of a Nicolet 6700 spectrometer (Thermo Fisher Scientific) equipped with an extended-range diamond ATR accessory. A catalyst-modified glassy carbon working electrode, an Ag/AgCl reference electrode, and a Pt wire counter electrode comprised the three-electrode configuration. Spectral data were gathered at 20 s intervals under potentiostatic control using chronoamperometry, with the applied potential swept from 0.95 to 1.45 V (vs. RHE).

The optical band gaps of the samples were determined using a Shimadzu UV-3600i Plus double-beam UV-Vis spectrophotometer. Their work functions were characterized by ultraviolet photoelectron spectroscopy (UPS) on a ThermoFisher Nexsa system.The UPS data analysis involved two key steps:

Valence Band Maximum (VBM): The VBM was identified by performing a linear fit to the leading edge of the valence band spectrum and extrapolating it to the baseline energy.

Work Function (Φ): The work function was calculated using the formula $\Phi = h\nu - (E_{cut\text{-}off} - E_F)$, where $h\nu$ is the incident photon energy (21.22 eV for He I). For example, with a measured secondary electron cut-off edge at 17.28 eV relative to the Fermi level, the work function is $\Phi = 21.22\ \text{eV} - 17.28\ \text{eV} = 3.94\ \text{eV}$.

1.3 Electrochemical characterizations

The electrochemical properties were characterized using a Biologic VMP3 workstation with a standard three-electrode setup in 1.0 M KOH (pH = 13.5). The system comprised a working electrode (1 cm² catalyst-coated nickel foam), a graphite rod counter electrode, and a saturated calomel electrode (SCE). All reported potentials were iR-compensated and referenced to the reversible hydrogen electrode (RHE) scale according to the equation $E_{RHE} = E_{SCE} + 0.059 \times pH + 0.241$ V.

All polarization curves were recorded at a scan rate of 5 mV $s^{-}1$ and were corrected for solution resistance (iR compensation). The uncompensated ohmic resistance (Rs ≈ 0.89 Ω) was determined from the high-frequency intercept of the electrochemical impedance spectra. An 85% iR compensation (corresponding to 0.76 Ω) was applied during the measurements using the potentiostat's built-in positive-feedback function.

Catalytic activity was evaluated by linear sweep voltammetry (LSV) from 0 to 1.4 V (vs. SCE) at a scan rate of 0.5 mV/s. The electrochemical active surface area (ECSA) was estimated via cyclic voltammetry (CV) in the non-Faradaic region (0.1–0.2 V vs. SCE) at scan rates ranging from 2 to 12 mV/s. The double-layer capacitance (C_{dl}) was derived from the slope of the charging current (j_a - j_c)/2 versus scan rate (v) plot, and ECSA was calculated as C_{dl}/C_s, where C_s is 40 μF cm^{-2}. The TOF values, reflecting the activity of a single catalytic site, were calculated by the equation: TOF= (j×A)/(4×F×n), where j represents the current density (A cm^{-2}) at an applied potential. The A stands for the working area of the electrode. Electrochemical impedance spectroscopy (EIS) was conducted at 0.5 V (vs. SCE) over a frequency range of 300 kHz to 10 mHz, with the resulting spectra fitted using ZSimDemo

software. Stability was assessed through chronopotentiometry at current densities of 10 and 100 mA cm^{-2}. Overall water splitting performance was measured by LSV from 0 to 2.5 V at 5 mV/s.

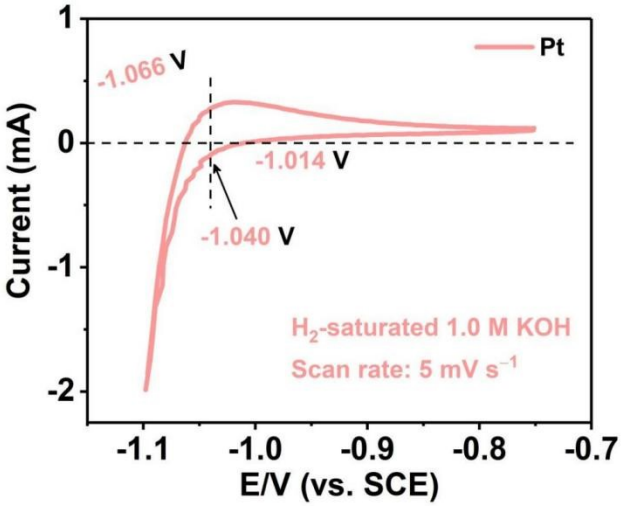

Fig. S1. RHE voltage calibration.

The reference hydrogen electrode (RHE) was calibrated in an H_2-saturated electrolyte with a platinum wire working electrode. By scanning at 5 mV/s, the thermodynamic potential for the hydrogen evolution reaction was determined from the average of the two zero-current potentials. As illustrated, the measured potential difference between $E_{(SCE)}$ and $E_{(RHE)}$ in 1.0 M KOH (pH = 13.6) was 1.040 V. This value is consistent with the theoretical difference calculated from the Nernst equation, $E_{(RHE)} = E_{(SCE)} + 0.241 + 0.059 \times pH$, which simplifies to 1.040 V under these conditions.

1.4 Faraday efficiency measurement using rotating ring-disk electrode (RRDE)

The charge efficiency toward the oxygen evolution reaction (OER) was assessed by a rotating ring-disk electrode (RRDE) method. The experiment employed a Pt-ring/glassy-carbon-disk electrode, with the catalyst (5 μL ink) deposited on the disk. Measurements were carried out in a N_2-purged 1 M KOH solution at a rotation speed of 1600 rpm. The disk electrode underwent polarization at a sweep rate of 5 mV s^{-1} to drive OER, while the ring electrode was

held at 0.4 V vs. RHE to quantitatively reduce the molecular oxygen reaching its surface.

The Faraday efficiency (FE) was then calculated using the following expression[1]:

$$FE = \frac{I_r/N}{I_d} \quad (1)$$

Where I_r and I_d represent the ring and disk currents, respectively, and (N = 0.37) is the predetermined collection efficiency of the RRDE. The efficacy of this approach is demonstrated by the observation of a 0.189 mA ring current upon applying a 0.518 mA disk current, confirming the selective detection of oxygen and validating the FE calculation.

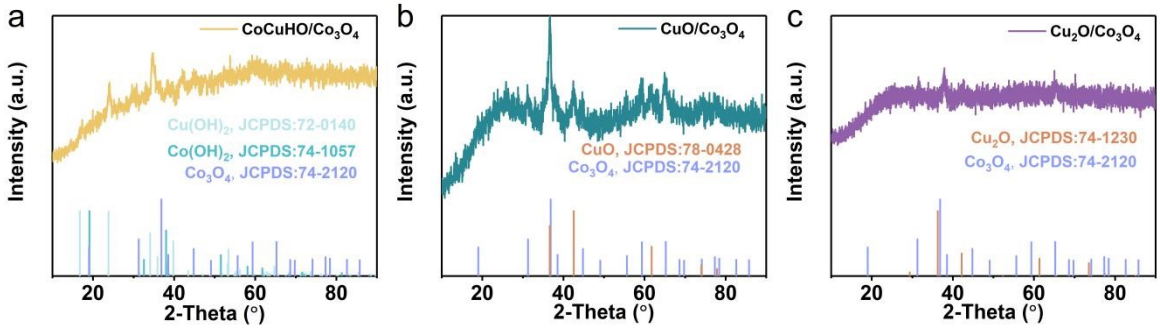

Fig. S2. XRD patterns of (a) $CoCuHO/Co_3O_4$@NF, (b) CuO/Co_3O_4@NF, (d) Cu_2O/Co_3O_4@NF.

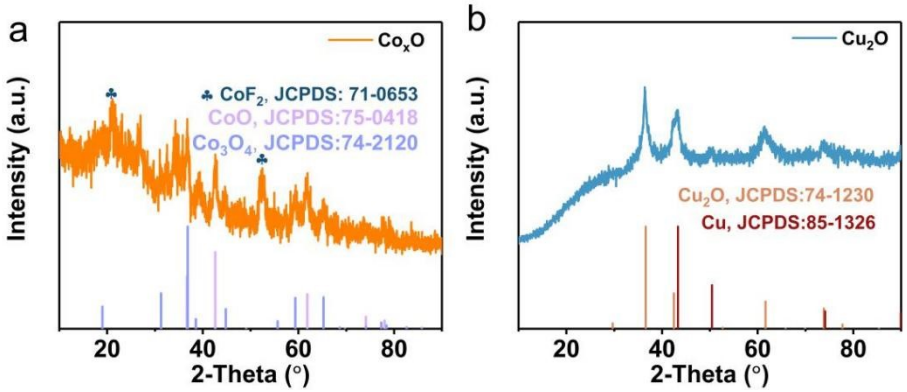

Fig. S3. XRD patterns of (a) Co_xO@NF, (b) Cu_2O@NF.

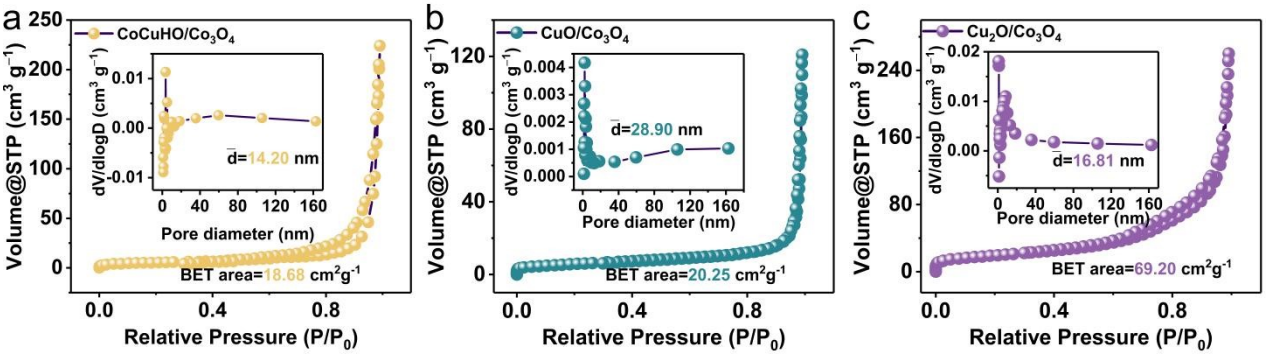

Fig. S4. N_2 adsorption/desorption isotherms and pore size distributions of (a) $CoCuHO/Co_3O_4$@NF, (b) CuO/Co_3O_4@NF, (d) Cu_2O/Co_3O_4@NF.

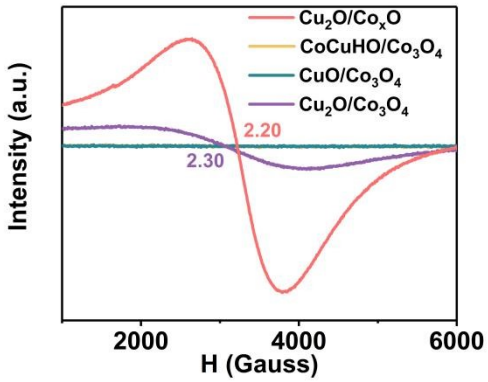

Fig. S5. EPR spectra of Cu_2O/Co_xO@NF, $CoCuHO@Co_3O_4$/NF, $CuO@Co_3O_4$/NF, and $Cu_2O@Co_3O_4$/NF.

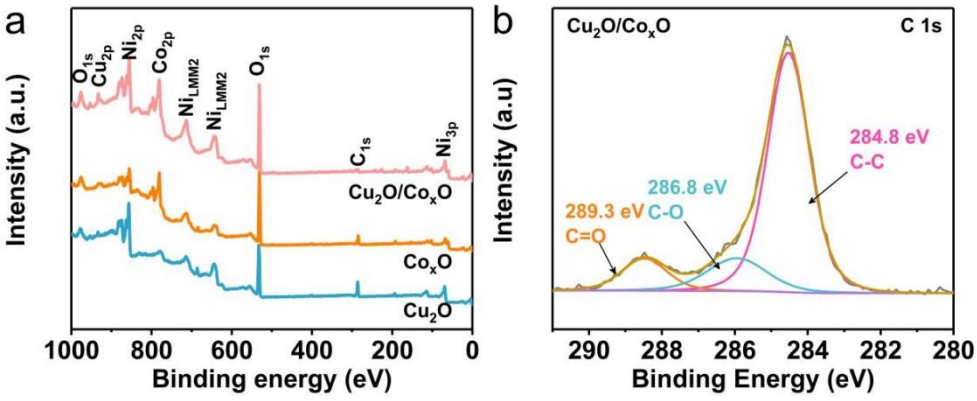

Fig. S6. XPS survey spectra (a) and high-resolution C 1*s* spectrum (b) of Cu_2O/Co_xO@NF.

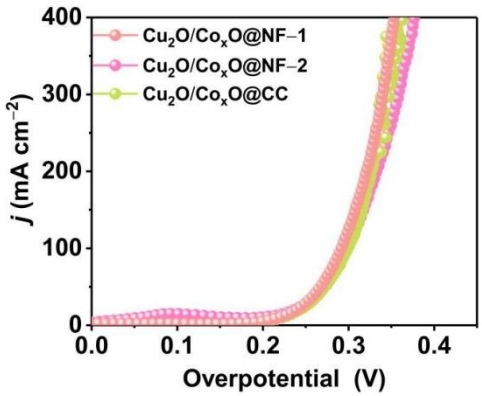

Fig. **S7.** Linear sweep voltammetry (LSV) curves of Cu_2O/Co_xO@NF catalysts prepared in different batches on nickel foam (NF) and carbon cloth (CC) substrates.

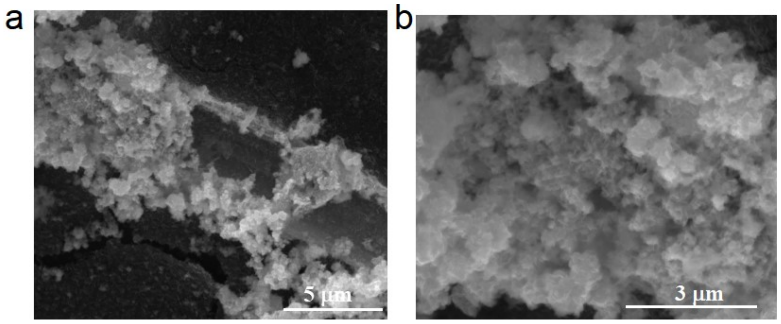

Fig. **S8.** SEM image of Cu_2O/Co_xO@CC.

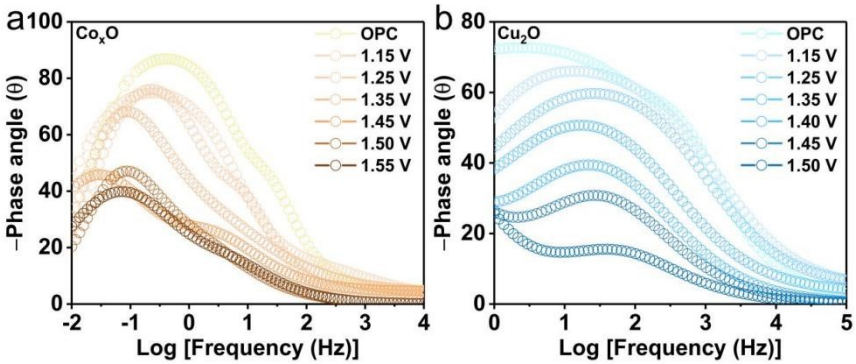

Fig. **S9.** Bode phase plots of (a) Co_xO@NF and (b) Cu_2O@NF at various potentials.

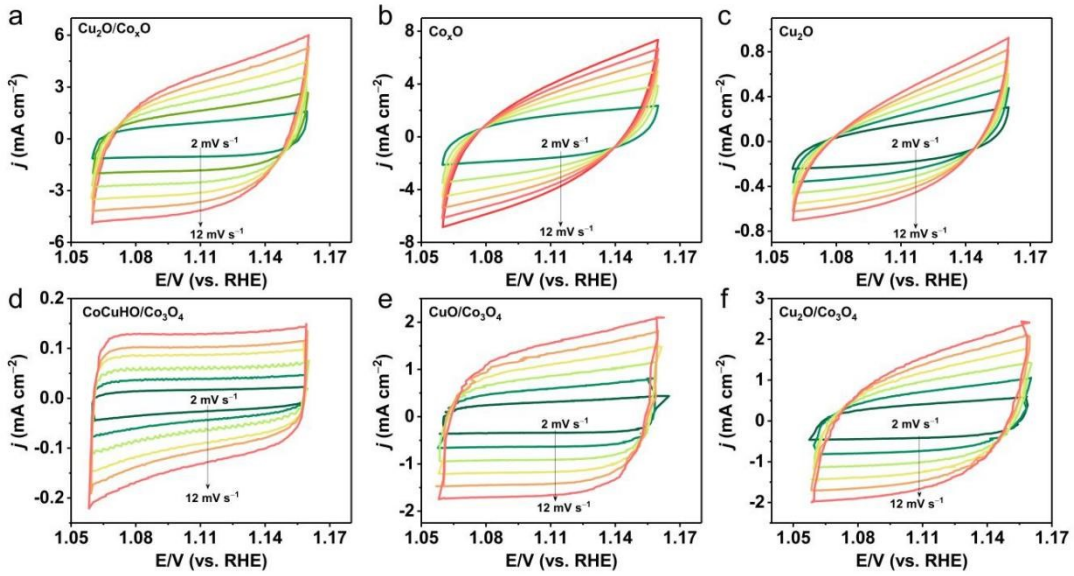

Fig. S10. Cyclic voltammograms (CVs) of (a) Cu_2O/Co_xO@NF, (b)Co_xO@NF, (c) Cu_2O@NF, (d) $CoCuHO/Co_3O_4$@NF, (e) CuO/Co_3O_4@NF and (f) Cu_2O/Co_3O_4@NF at a scan rate of 2, 4, 6, 10 and 12 mV s^{-1}.

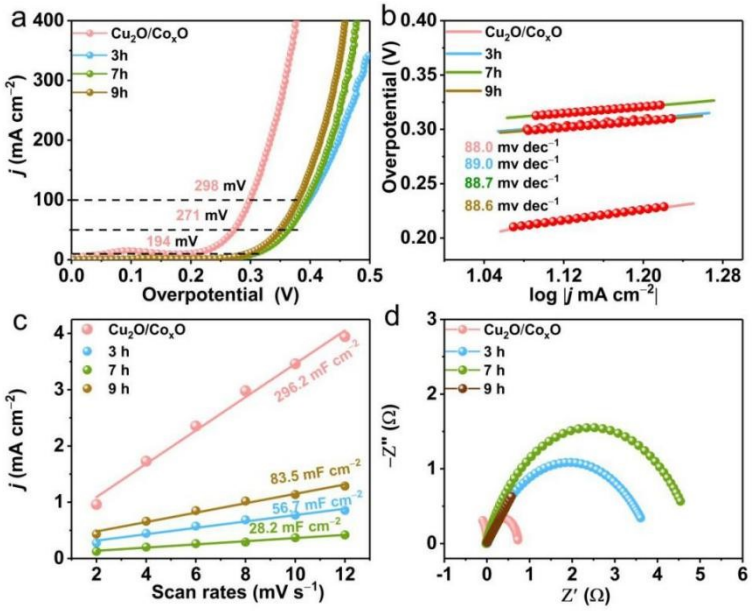

Fig. S11. OER performance of Cu_2O/Co_xO@NF catalysts synthesized with different phytic acid etching times (3h, 7h, and 9h). (a) Polarization curves at a scan rate of 0.5 mV s^{-1}, (b) Tafel slopes, (c) Double-layer capacitance (C_{dl}) plots, and (d) Nyquist plots of different catalysts in 1.0 M KOH solution.

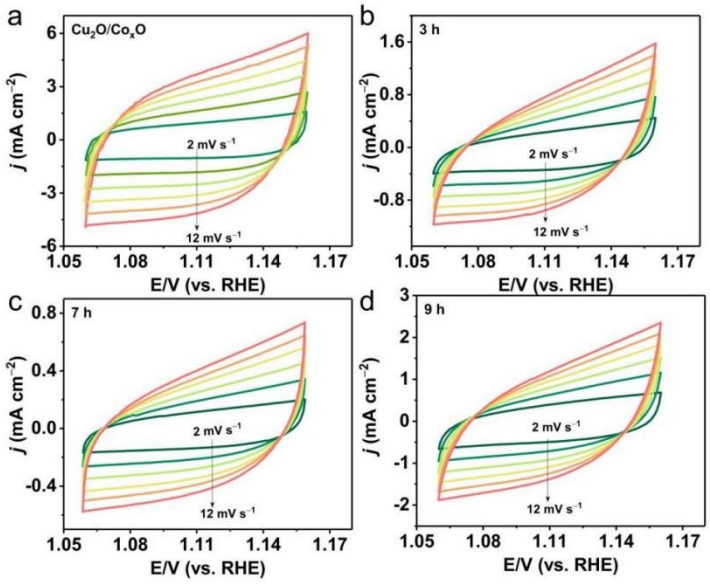

Fig. S12. Cyclic voltammograms (CVs) of Cu_2O/Co_xO@NF catalysts synthesized with different phytic acid etching times (3h, 7h, and 9h) with scan rates of 2, 4, 6, 10, and 12 mV s^{-1} in 1.0 M KOH. (a) 5h, (b) 3h, (c) 7h, and (d) 9h.

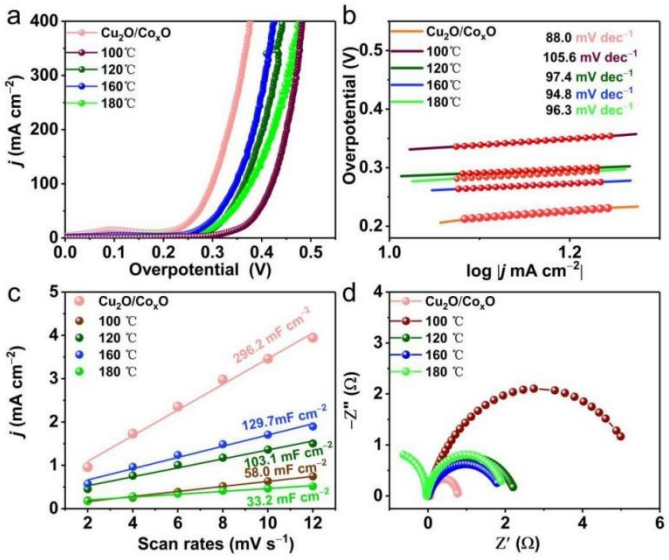

Fig. S13. OER performance of Cu_2O/Co_xO@NF catalysts synthesized at different hydrothermal reaction temperatures (100°C, 120°C, 160°C, and 180°C). (a) Polarization curves with a scan rate of 0.5 mV s^{-1}, (b) Tafel slopes, (c) Double-layer capacitance (C_{dl}) plots, and (d) Nyquist plots of different catalysts in 1.0 M KOH solution.

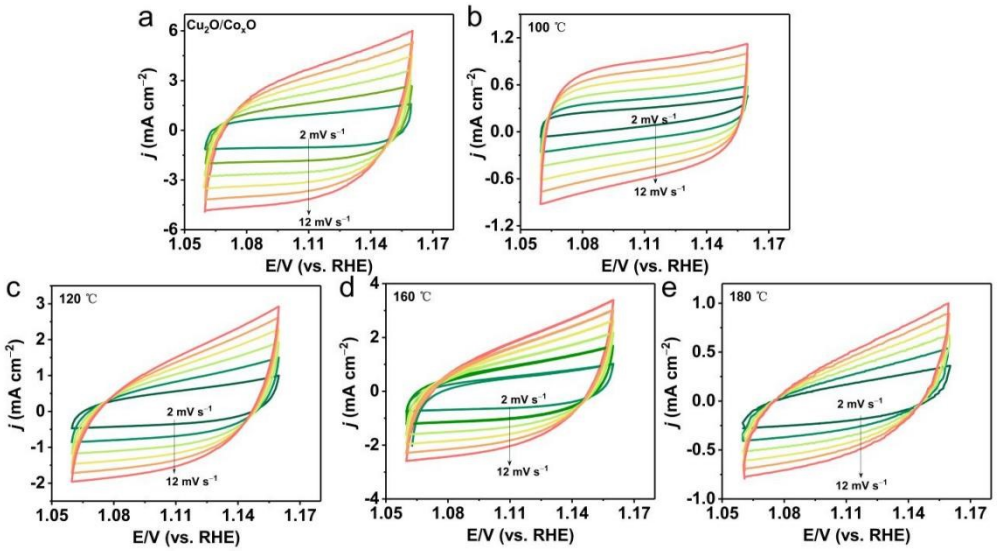

Fig. S14. Cyclic voltammograms (CVs) of Cu_2O/Co_xO@NF catalysts synthesized at different temperatures measured at scan rates from 2 to 12 mV s^{-1} for C_{dl} determination. (a) 100°C, (b) 120°C, (c) 160°C, and (d) 180°C.

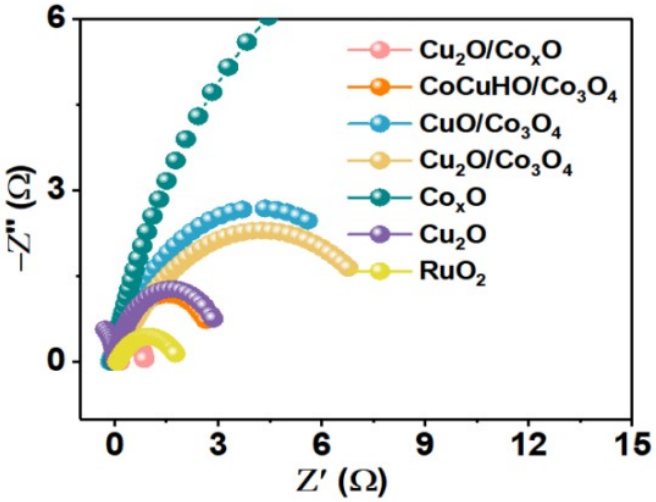

Fig. **S15.** Nyquist plots for different catalysts.

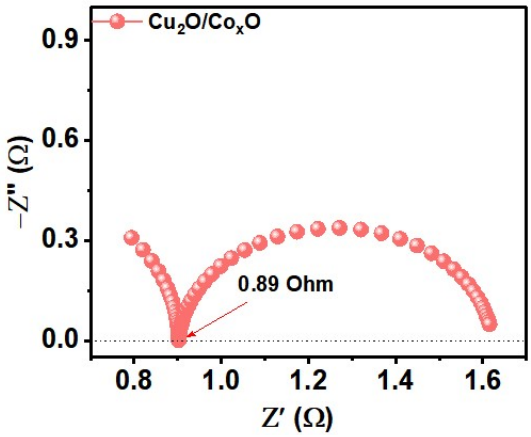

Fig. S16. Electrochemical impedance spectrum (Nyquist plot) of Cu_2O/Co_xO@NF in 1 M KOH, with high-frequency intercept (inset) defining the solution resistance (R_s = 0.89 Ω).

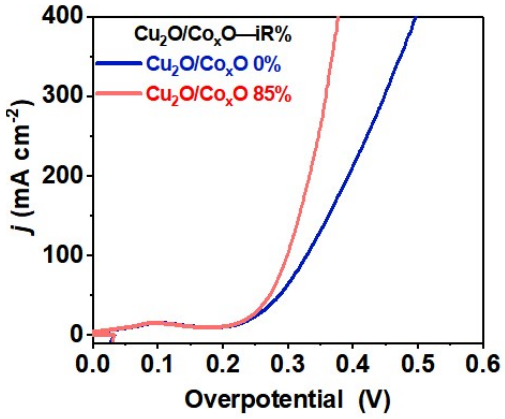

Fig. S17. Comparison of raw (uncompensated) and iR-corrected (85%) linear sweep voltammetry curves for OER on Cu_2O/Co_xO@NF in 1 M KOH.

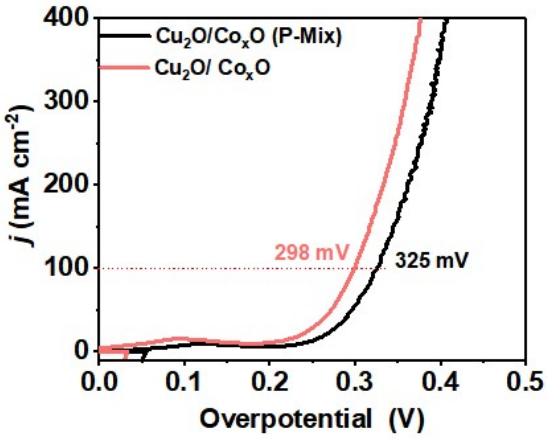

Fig. S18. Comparison of OER performance between the Cu_2O/Co_xO@NF and the Cu_2O/Co_xO@NF(P-Mix).

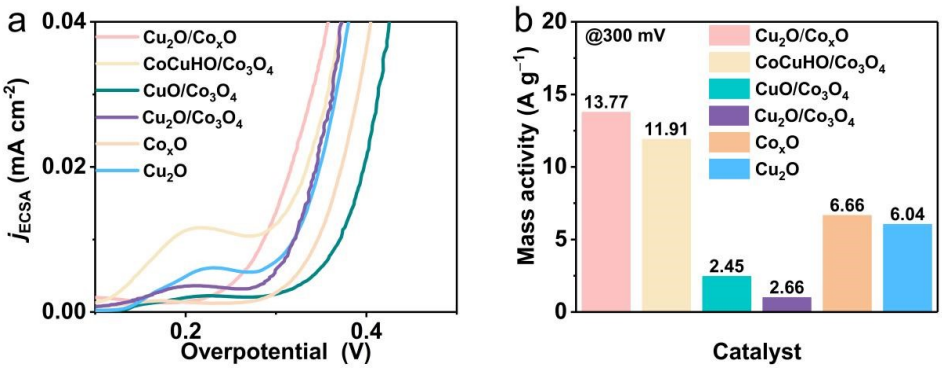

Fig. **S19.** (a) ECSA-normalized LSV curves. (b) OER mass activity at 300 mV.

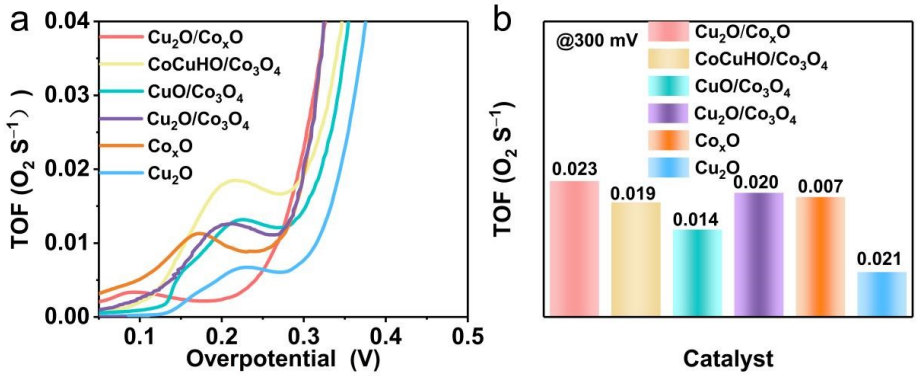

Fig. **S20.** (a) Turnover frequency values. (b) The TOF values at 350 mV.

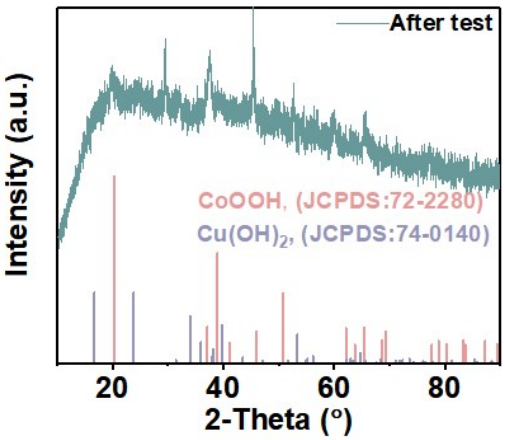

Fig. S21. XRD pattern of the Cu_2O/Co_xO@NF catalyst after oxygen evolution reaction stability test.

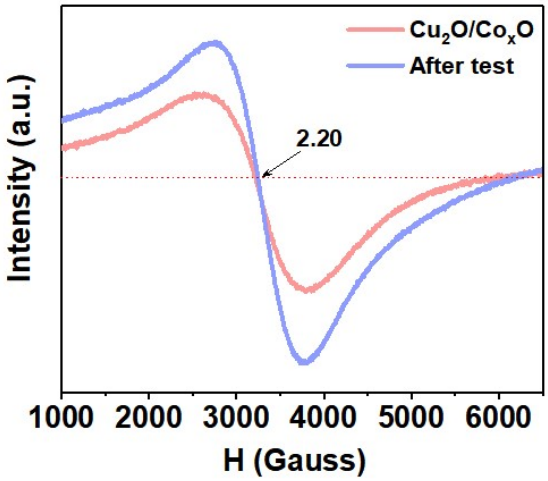

Fig. S22. EPR spectra of Cu_2O/Co_xO@NF before and after 450 h OER.

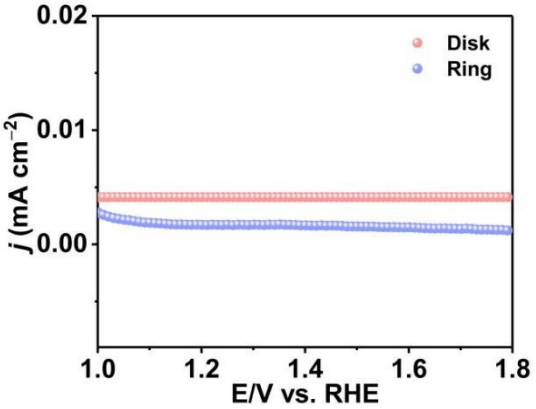

Fig. S23. Disk and ring currents of the Cu_2O/Co_xO@NF@NF nanoalloy measured in 1.0 M KOH using a rotating ring-disk electrode (RRDE) at 1600 rpm.

Table S1. Comparison of design strategies and OER performance of representative cobalt-copper-based electrocatalysts.

Catalyst	Design Strategy / Key Feature	Key Distinction from This Work	Reference
Cu_2O/Co_xO	**Built-in electric field and defect synergy mechanism**	**Demonstrates the synergy between directional charge field and atomic-scale defects**	**This work**
CuO_x/Co_3O_4 heterostructures	The mechanism of stabilizing lattice oxygen at heterogeneous interfaces	The interface is used to stabilize specific reaction mechanisms; lacks intentional BIEF-defect coupling	2
CoO/Co_3O_4-CuO nanohybrid	Macroscopic-microstructure engineering	Structural Engineering Optimization for Mass Transfer and Electrical Conductivity;lacks intentional BIEF-defect coupling	3

Table S2. Quantitative assessment of metal dissolution for the Cu_2O/Co_xO@NF catalyst during at 100 mA/cm^2 for 400 h OER stability test.

Element	100 h Total Dissolution (g)	200 h Total Dissolution (g)	300 h Total Dissolution (g)	400 h Total Dissolution (g)
Cobalt (Co)	6.47092×10^{-5}	7.70662×10^{-5}	8.43262×10^{-5}	9.65262×10^{-5}
Copper (Cu)	5.10766×10^{-5}	6.88716×10^{-5}	7.90516×10^{-5}	8.96916×10^{-5}
Total Dissolution	1.157858×10^{-4}	1.459378×10^{-4}	1.633778×10^{-4}	1.862178×10^{-4}
Dissolution Ratio	1.48%	1.87%	2.09%	2.38%

Table S3. The metal contents in different catalysts were determined by ICP-MS.

Catalyst	Co (wt%)	Cu (wt%)
Cu_2O/Co_xO@NF	**32.17**	**65.81**
Co_xO@NF	62.29	None
Cu_2O@NF	None	86.25
CoCuHO/Co_3O_4@NF	45.12	52.42
CuO/Co_3O_4@NF	46.33	51.06
Cu_2O/Co_3O_4@NF	42.04	55.49

Table S4. Summary of previously reported outstanding transition metal OER catalysts in alkaline solutions.

Catalyst	η_{100} (mV)	Tafel slope (mV dec^{-1})	Reference
Cu_2O/Co_xO@NF	**298**	**88**	**This work**
Co_3Cu-Ni_2MNs	390	87	[4]
Ru, Ni-CoP	360	102.3	[5]
NW-$MnCo_2O_4$/GD	482	111	[6]
CoP/MoP@C,N	390	97	[7]
CoCe-MOF/CP	455	96.1	[8]
Mo-CoMOF@NF	324	96	[9]
Co-Mo-0.005–6N	357	106	[10]
NiCo-LDHs/NiCoS	308	62	[11]
c-$CoSe_2$-CoN/NC	490	97	[12]
FeCoLDH/NF	338	83	[13]
$CoMoS_x$/NF	345	92	[14]
(Fe,Co)OOH/MI	290	73	[15]
Co/Co_3O_4/CoF_2@NSC	370	88	[16]
LQNMP-Co_2O_3	320	54	[17]
CuO_x/Co_3O_4	308	43.5	[2]

Table S5. Overall water splitting performances of different catalysts in 1.0 M KOH electrolyte.

Cathodic || Anodic catalysts	Electrolyte	Cell voltage (V)	Reference
Cu_2O/Co_xO@NF||Pt-C@NF	**1.0 M KOH**	**1.54 V**	**This work**
Co-Ni-P	1.0 M KOH	1.64 V	[18]
CoRu-O/A@HNC-2	1.0 M KOH	1.558 V	[19]
CoFe-P/NF	1.0 M KOH	1.58 V	[20]
Cr-CoP/CP	1.0 M KOH	1.59 V	[21]
$Fe_{0.14}Co_{0.86}$ -P/CC	1.0 M KOH	1.63 V	[22]
$RuNi_1Co_1$@CMT	1.0 M KOH	1.58 V	[23]
NiFeLDH@NiCoP/NF	1.0 M KOH	1.90 V	[24]
Ru-NiO/Co_3O_4	1.0 M KOH	1.555 V	[25]
$CoSe_2$/$FeSe_2$	1.0 M KOH	1.60 V	[26]
Mo, Fe-NiCoP/NF	1.0 M KOH	1.545 V	[27]
Cu_3P/Ni_2P@CF	1.0 M KOH	1.56 V	[28]

Table S6. E-factor comparison of Cu_2O/Co_xO and RuO_2 syntheses.

Catalyst	Synthesis Process	E-factor ($g \cdot g^{-1}$)	Waste & Process Features
Cu_2O/Co_xO	Lab-scale one-pot aqueous hydrothermal	4.34	Only H_2O as waste; no toxic solvents/gases; earth-abundant metal salt raw materials
RuO_2	Lab-scale hydrolysis-calcination ($RuCl_3 \cdot 3H_2O$ precursor)	1.36	Waste: crystal water, toxic HCl gas, reaction-consumed H_2O; precious metal precursor
RuO_2	Industrial chlorination-roasting	12.60	Abundant Cl-containing waste gas/acidic wastewater; alkali residue from tail gas treatment; high energy consumption; precious metal purification waste

References

1. S. Zhao, Y. Wang, J. Dong, C.-T. He, H. Yin, P. An, K. Zhao, X. Zhang, C. Gao, L. Zhang, J. Lv, J. Wang, J. Zhang, A. M. Khattak, N. A. Khan, Z. Wei, J. Zhang, S. Liu, H. Zhao and Z. Tang, *Nat. Energy*, 2016, **1**, 16184.
2. C. Jia, Y. Chen, C. Zhou, X. Xiang, X. Long, B. Zhao, N. Zhang, S. Zhao, L. Chai, X. Liu and Z. Lin, *ACS Nano*, 2025, **19**, 19938-19950.
3. H. Liu, Z. Li, J. Hu, Z. Qiu, W. Liu, J. Lu and J. Yin, *Chem. Eng. J.*, 2022, **435**, 134995.
4. P. Dong, Y. Gu, G. Wen, R. Luo, S. Bao, J. Ma and J. Lei, *Small*, 2023, **19**, 2301473.
5. Y. Song, J. Cheng, J. Liu, Q. Ye, X. Gao, J. Lu and Y. Cheng, *Appl. Catal. B: Environ.*, 2021, **298**, 120488.
6. L. Qi, Z. Zheng, C. Xing, Z. Wang, X. Luan, Y. Xue, F. He and Y. Li, *Adv. Funct. Mater.*, 2022, **32**, 2107179.
7. D. Sun, S. Lin, Y. Yu, S. Liu, F. Meng, G. Du and B. Xu, *J. Alloys Compd.*, 2022, **895**, 162595.
8. Y. Liao, Y. Xiao, Z. Li, X. Zhou, J. Liu, F. Guo, J. Li and Y. Li, *Small*, 2024, **20**, 2307685.
9. N. Sun, X. Si, X. Wei, X. Zhou, H. Yu, F. Ding, X. Kong and Y. Sun, *Small*, 2025, **21**, 2407933.
10. X. Zhang, A. Wu, D. Wang, Y. Jiao, H. Yan, C. Jin, Y. Xie and C. Tian, *Appl. Catal. B: Environ.*, 2023, **328**, 122474.
11. J. Li, L. Wang, H. He, Y. Chen, Z. Gao, N. Ma, B. Wang, L. Zheng, R. Li, Y. Wei, J. Xu, Y. Xu, B. Cheng, Z. Yin and D. Ma, *Nano Res.*, 2022, **15**, 4986-4995.
12. X. Xu, X. Wang, S. Huo, X. Liu, X. Ma, M. Liu and J. Zou, *Adv. Mater.*, 2024, **36**, 2306844.
13. T. Tang, Z. Jiang, J. Deng, S. Niu, Z.-C. Yao, W.-J. Jiang, L.-J. Zhang and J.-S. Hu, *Nano Res.*, 2022, **15**, 10021-10028.
14. X. Shan, J. Liu, H. Mu, Y. Xiao, B. Mei, W. Liu, G. Lin, Z. Jiang, L. Wen and L. Jiang, *Angew. Chem. Int. Ed.*, 2020, **59**, 1659-1665.
15. W. Huang, J. Li, X. Liao, R. Lu, C. Ling, X. Liu, J. Meng, L. Qu, M. Lin, X. Hong, X. Zhou, S. Liu, Y. Zhao, L. Zhou and L. Mai, *Adv. Mater.*, 2022, **34**, 2200270.
16. H. Li, G. Yan, H. Zhao, P. C. Howlett, X. Wang and J. Fang, *Adv. Mater.*, 2024, **36**, 2311272.
17. Z. Fan, Q. Sun, H. Yang, W. Zhu, F. Liao, Q. Shao, T. Zhang, H. Huang, T. Cheng, Y. Liu, M. Shao, M. Shao and Z. Kang, *ACS Nano*, 2024, **18**, 5029-5039.
18. L. Chai, S. Liu, S. Pei and C. Wang, *Chem. Eng. J.*, 2021, **420**, 129686.
19. G. Li, K. Zheng, W. Li, Y. He and C. Xu, *ACS Appl. Mater. Interfaces*, 2020, **12**, 51437-51447.
20. D. Duan, D. Guo, J. Gao, S. Liu and Y. Wang, *J. Colloid Interface Sci.*, 2022, **622**, 250-260.
21. W. Li, Y. Jiang, Y. Li, Q. Gao, W. Shen, Y. Jiang, R. He and M. Li, *Chem. Eng. J.*, 2021, **425**, 130651.
22. H. Yu, L. Qi, Y. Hu, Y. Qu, P. Yan, T. T. Isimjan and X. Yang, *J. Colloid Interface Sci.*, 2021, **600**, 811-819.

23. Y. Xue, Q. Yan, X. Bai, Y. Xu, X. Zhang, Y. Li, K. Zhu, K. Ye, J. Yan, D. Cao and G. Wang, *J. Colloid Interface Sci.*, 2022, **612**, 710-721.
24. H. Zhang, X. Li, A. Hähnel, V. Naumann, C. Lin, S. Azimi, S. L. Schweizer, A. W. Maijenburg and R. B. Wehrspohn, *Adv. Funct. Mater.*, 2018, **28**, 1706847.
25. J. Zhang, J. Lian, Q. Jiang and G. Wang, *Chem. Eng. J.*, 2022, **439**, 135634.
26. F. O. Boakye, Y. Li, K. A. Owusu, I. S. Amiinu, Y. Cheng and H. Zhang, *Mater. Chem. Phys.*, 2022, **275**, 125201.
27. X. An, L. Quan, J. Liu, Q. Tang, H. Lan and H. Liu, *J. Colloid Interface Sci.*, 2022, **615**, 456-464.
28. H. Liu, J. Gao, X. Xu, Q. Jia, L. Yang, S. Wang and D. Cao, *Chem. Eng. J.*, 2022, **448**, 137706.